# Flow around a hemisphere-cylinder at high angle of attack and low Reynolds number. Part I: Experimental and numerical investigation

Soledad Le Clainche [a], Jingyun I. Li [b], Vassilis Theofilis [a], Julio Soria [b,c]

[a] School of Aeronautics, Universidad Politécnica de Madrid, Spain
[b] Laboratory for Turbulence Research in Aerospace and Combustion, Department of Mechanical and Aerospace Engineering, Monash University, Australia
[c] Department of Aeronautical Engineering, King Abdulaziz University, Saudi Arabia

A B S T R A C T

Three-dimensional Direct Numerical Simulations combined with Particle Image Velocimetry experiments have been performed on a hemisphere-cylinder at Reynolds number 1000 and angle of attack 20°. At these flow conditions, a pair of vortices, so-called "horn" vortices, are found to be associated with flow separation. In order to understand the highly complex phenomena associated with this fully three-dimensional massively separated flow, different structural analysis techniques have been employed: Proper Orthogonal and Dynamic Mode Decompositions, POD and DMD, respectively, as well as critical-point theory. A single dominant frequency associated with the von Karman vortex shedding has been identified in both the experimental and the numerical results. POD and DMD modes associated with this frequency were recovered in the analysis. Flow separation was also found to be intrinsically linked to the observed modes. On the other hand, critical-point theory has been applied in order to highlight possible links of the topology patterns over the surface of the body with the computed modes. Critical points and separation lines on the body surface show in detail the presence of different flow patterns in the base flow: a three-dimensional separation bubble and two pairs of unsteady vortices systems, the horn vortices, mentioned before, and the so-called "leeward" vortices. The horn vortices emerge perpendicularly from the body surface at the separation region. On the other hand, the leeward vortices are originated downstream of the separation bubble, as a result of the boundary layer separation. The frequencies associated with these vortical structures have been quantified.

## 1. Introduction

Flow separation over inclined axisymmetric bodies affects stability and control of the object. Due to various industrial applications, such as aircraft fuselages and submarines, to study the flow around a hemisphere-cylinder model at both zero and non-zero angles of attack has been the subject of several experimental and computational investigations. The main goal of such studies was to understand flow patterns in the vicinity of the nose region. Separation around the nose is a prototype of essentially three-dimensional laminar flow separation. The qualitative physical picture emerging is a laminar separation bubble, which at high incidence of the body results in a pair of vortices, so-called "Horn" vortices. As the Reynolds number increases, these vortices emerge from the nose of the body and affect vehicle stability, owing to their unsteady nature. Finally, convective effects cause separation bubble to develop and boundary layer to separate and roll up downstream generating the so-called "Leeward" vortices.

Hsieh [18] was the first to study the flow around a hemisphere cylinder at zero incidence in low supersonic flow and the effect of Mach number in the separation bubble. Fairlie [10] studied prolate-spheroid and hemisphere-cylinder geometries in incompressible flow at high angle of attack ($AoA$) and Reynolds number ($Re$) $10^6$. He found for the first time in the hemisphere-cylinder the origin of the horn vortices emerging from the body surface when the angle of attack was higher than 17.5°. Two spiral nodes symmetrically placed about the leeward plane of symmetry, giving rise to a quite strong vortex pair shed downstream.

A sequence of experiments performed in the early 1980s using surface hot-film sensors [29,24] and laser-Doppler velocimetry [19, 7,6] revealed a pair of vortices on the leeward region far from the body nose, the leeward vortices. Hsieh [19], Costis et al. [6] and Costis and Telionis [7] were studying the origin of such vortices and the effects of transition on its development. It was postulated that effects of boundary layer transition cause the development of

vortices sheets to form this pair of vortices. Hsieh and Wang [20] provided numerical evidence in supporting this flow pattern.

Another series of investigations were carried out in order to study the three-dimensional complex topology patterns developed above the body surface, based on critical-point theory introduced by Dallmann [8] and Perry and Chong [35]. Tobak and Peake [50,49,34], as well as Hornung and Perry [17] and Perry and Hornung [36] identified critical points and separation lines on the hemisphere-cylinder body surface. They identified the critical points defining the separation bubble (two unstable foci associated with the origin of the horn vortices, the saddle point of separation, the node point of re-attachment and two saddles symmetrically positioned respect to the symmetry plane) and the primary and secondary lines of separation related to the leeward vortices. Several authors followed up to contribute in such research [28,56,54] identifying experimentally this flow pattern on the hemisphere-cylinder at different flow regimes.

Ying et al. [55] demonstrated numerically the asymmetricity of horn vortices, while Hoang et al. [14,15], who experimentally studied the influence of Reynolds number and angle of attack on this pair of vortices, did not find evidence of such asymmetry. However, the latter authors found the lack of connectivity between the nose structures and the separation lines, which give rise to the vortical structures over the aft part of the body.

More recently Gross et al. [13] performed direct numerical simulations at moderate Reynolds numbers ($Re = 2000$ and $Re = 5000$) and moderate-high incidence. They identified the existence of a shear layer instability on the symmetry plane at low incidence ($AoA = 10^\circ$). They suggested that the dominant mechanism in flow separation was an inviscid (linear) shear layer instability. On the other hand, Bohorquez et al. [4] and Sanmiguel-Rojas et al. [43] performed direct numerical simulations on the same geometry at $AoA = 0^\circ$ finding the bifurcations of the linear global stability modes on the wake of the hemisphere-cylinder as a function of the Reynolds number and the aspect ratio of the body (length/diameter). A global mode with non-dimensional frequency Strouhal number $St \simeq 0.12$ was associated with the von Karman vortex shedding. The same mode was found by many authors that studied flow past bluff bodies [51,44] and the influence of angle of attack on slim bodies [39,38]. Sanmiguel-Rojas et al. [42] contributed numerically to the study of the flow around a hemisphere-cylinder, analyzing the effect of a blunt-base on the hemisphere-cylinder and applying flow control. Finally, Jiménez-González et al. [21] performed numerical simulations of the flow past a spinning hemisphere-cylinder, focusing their study on the evolution of the forces and flow regimes as a function of Reynolds number and the dimensionless angular velocity.

From the previous discussion it is to be expected that three-dimensional flow separation gives rise to rather complex flow structural patterns. Finding the global instabilities that dominate the flow separation phenomenon is still nowadays an open topic. In the absence of the identification of linear critical stability limits, the first type of structural flow analysis to be performed is based on finding the most energetic Proper Orthogonal Decomposition (POD) modes [32,33]. Additionally, Rowley et al. [40] present Koopman modes as a complement for POD modes. DMD algorithm presented by Schmid [45] provides an approximation of Koopman modes. Although DMD [30,31] may not be the optimal algorithm to describe the dynamic of very complex systems [5], it is a relatively inexpensive technique in terms of computational cost that may detect global modes on periodic saturated nonlinear systems [1]. Therefore, POD and DMD techniques have been applied in this work as complement to the topological study provided by critical-point theory, in order to detect global instabilities on the hemisphere-cylinder related with flow separation and flow topology patterns.

This article combines Direct Numerical Simulations (DNS) and Particle Image Velocimetry (PIV) experiments to contribute in the study of flow separation and the shear layer effects over a hemisphere-cylinder. In order to study frequencies and flow structures around the body, three-dimensional DNS has been carried out at Reynolds number 1000 and angle of attack 20° over a hemisphere-cylinder with aspect ratio $L/D = 8$ ($L$ and $D$ are the length and diameter of the body respectively). In addition, Particle Image Velocimetry experiments have been performed over the same geometry at the same flow conditions. Frequencies and structures have been detected employing critical point theory, Power Spectral Density analysis (PSD), Proper Orthogonal Decomposition (POD) and Dynamic Mode Decomposition (DMD). Section 2 briefly discusses the theory of the different structural analysis techniques that have been applied in order to determine coherent structures and their associated frequencies. Section 3 briefly discusses the numerical method and code employed to solve the DNS. Section 4 presents the experimental facility and conditions settings for the experiments that were carried out. Finally Section 5 and Section 6 present the results and the conclusions of this work, respectively.

## 2. Structural analysis theory

Transitional and turbulent flows exhibit complex behaviors, which motivates the use of visualization and structural analysis techniques in order to understand their nature. Coherent structure analysis is a concept used to describe patterns that are present with a certain frequency in a flow. Several approaches exist to identify and to describe coherent structures. In particular, in this paper Critical Point Theory [8,35] has been employed to describe and understand the features of the fluid motion. In addition, Proper Orthogonal Decomposition [46,32] and Dynamic Mode Decomposition [40,45] have been used, in order to describe structures as an expansion of modes associated with different frequencies.

### 2.1. Critical point theory

Critical point theory is a technique introduced by Dallman [8] and Perry and Chong [35] to describe the topological features of flow patterns. The idea is to use a Taylor series to expand the flow around a critical point. A critical point is a location in space where the three components of velocity vector are all simultaneously zero. If only the linear terms of the Taylor expansion are considered, this flow expansion can be represented via the Jacobian matrix of velocity $J$

$$\begin{pmatrix} \dot{x} \\ \dot{y} \\ \dot{z} \end{pmatrix} = \begin{pmatrix} j_{11} & j_{12} & j_{13} \\ j_{21} & j_{22} & j_{23} \\ j_{31} & j_{32} & j_{33} \end{pmatrix}, \begin{pmatrix} x \\ y \\ z \end{pmatrix} \tag{1}$$

written in compact form as

$$\dot{x} = Jx, \tag{2}$$

where $x$, $y$, $z$ are the spatial coordinates, $\dot{x}$, $\dot{y}$, $\dot{z}$ its time derivatives, $J$ is the Jacobian matrix, $P = -\mathrm{tr}(J)$, $Q = \Delta J$ and $R = -\det(J)$ (in incompressible flow $P = 0$).

The eigenvalues of the Jacobian matrix satisfy the equation:

$$\lambda^3 + P\lambda^2 + Q\lambda + R = 0. \tag{3}$$

Depending on the nature of the eigenvalues, $\lambda$, critical points are classified as node, saddle, focus and a sequence of borderline cases. Nodal and focal points can be either stable or unstable, depending on whether the streamlines are attracted towards or repelled from the critical point, respectively. Fig. 1 summarizes the different types of critical points for a two-dimensional case (critical points obtained on a plane) [53].

| Critical Point | $\lambda_1$ | $\lambda_2$ | | |
|---|---|---|---|---|
| Saddle | $\sigma_1>0$ | $\sigma_2<0$ | $\sigma_1=-\sigma_2$ |  |
| Node sink | $\sigma_1<0$ | $\sigma_2<0$ | $\sigma_1\neq\sigma_2$ |  |
| Focus sink | $\sigma_1<0$ | $\sigma_2<0$ | $\sigma_1=\sigma_2$ |  |
| Spiral sink | $\sigma+i\omega$ | $\sigma-i\omega$ | $\sigma<0$ |  |
| Node source | $\sigma_1>0$ | $\sigma_2>0$ | $\sigma_1\neq\sigma_2$ |  |
| Focus source | $\sigma_1>0$ | $\sigma_2>0$ | $\sigma_1=\sigma_2$ |  |
| Spiral source | $\sigma+i\omega$ | $\sigma-i\omega$ | $\sigma>0$ |  |
| Center | $i\omega$ | $-i\omega$ | $\sigma=0$ |  |

**Fig. 1.** Classification of critical points on a two-dimensional case.

In the case of critical points at a wall (zero velocity), or no-slip points, the Jacobian matrix elements are composed by the wall-stress tensor. The permissible connections between univocal critical points became defined by the streamlines [39].

The work of Rodríguez and Theofilis [38,39] was the first to relate critical points formation with linear amplification of global modes of instability in separated flow. In particular, they studied the adverse-pressure gradient boundary layer flow on a flat plate and the massively separated flow over a two-dimensional airfoil, respectively.

Motivation thus exists to employ critical point theory to identify the surface critical points present in the hemisphere-cylinder and their associated three-dimensional flow structures, frequencies and instabilities.

### 2.2. Proper Orthogonal Decomposition

Application of the Karhunen–Loève theory, also known in different fields of Computational Mechanics as Proper Orthogonal Decomposition (POD) [16] and Principal Component Analysis (PCA) [22,25], permits to describe dynamical flow structures that occurred systematically. By solution of an eigenvalue problem, POD permits the reduction of large space–time collections of numerical or experimental laminar or turbulent flow fields. A small number of POD modes suffices to capture the relevant physics of the flow, making POD a useful technique in the formulation of Reduced Order Models (ROM).

For the construction of the POD eigensystem it is not necessary to have full knowledge of the dynamical operator. There exist two different methods to compute POD: the classic and the snapshots method. The classic method [27] generates a matrix eigenvalue problem of large dimension considering the ensemble-averaged correlation between the velocity components of a data set. The snapshots method [46] builds a correlation matrix as the application of the inner product to the pairs of temporal instants of velocity vector. The formed matrix is in this case smaller making the eigenvalue problem more tractable. Therefore, POD snapshots method has been employed on this paper.

POD is a statistical technique that delivers a basis of orthogonal eigenfunctions. The idea behind POD analysis is to find an orthogonal basis function $\psi^k(\mathbf{x})$ that most faithfully represents a random vector function, $\mathbf{u}(\mathbf{x},t)$ using the form:

$$\mathbf{u}(\mathbf{x},t) \simeq \sum_{k=1}^{K} a^k(t)\psi^k(\mathbf{x}) \tag{4}$$

where $a^k(t)$ is a time dependent expansion coefficient. The least square error of this projection is minimum. This optimization problem for $\psi^k(\mathbf{x})$ leads to the eigenvalue problem of a cross-correlation tensor $\mathbf{R}$. The cross-correlation tensor is defined as the standard inner product for vector functions in the following way

$$R_{ij} = \langle \mathbf{u}^j, \mathbf{u}^i \rangle = \int_D \mathbf{u}^j \cdot \mathbf{u}^i d\mathbf{x} \tag{5}$$

where $\mathbf{u}^i \equiv \mathbf{u}(\mathbf{x}, t_i)$ is a given sequence of instantaneous data and $\mathbf{R}$ is a compact self-adjoint operator [16].

The POD modes (optimal functions $\psi^k(\mathbf{x})$) are then obtained as the projection of the eigenvectors of $\mathbf{R}$ over the snapshots matrix composed by the instantaneous flow field. The time-dependent projection weights $a_k(t)$ in (4) are obtained from

$$a^k(t) = \int_D u(\mathbf{x},t)\psi^k(\mathbf{x})d\mathbf{x}. \tag{6}$$

In this article POD is applied to the fluctuating velocity field, thus the mean velocity is subtracted from the instantaneous data. By definition of Eq. (5), POD modes are associated with correlations of fluctuating kinetic energy. The percentage of energy contained in each POD mode $i$ in a system of $N$ modes is defined as:

$$E(\%) = \frac{\lambda^i}{\sum_{i=1}^{N}\lambda^i} \cdot 100 \tag{7}$$

where $\lambda^i$ are the eigenvalues of the cross-correlation matrix $\mathbf{R}$. The eigenvalues (and their corresponding eigenvectors) are ordered according to the higher magnitude of correlation (kinetic energy)

$$\lambda^1 > \lambda^2 > \ldots > \lambda^N = 0 \tag{8}$$

One of the mostly attractive features contained in POD modes is that, unlike the global eigenmodes (linear stability analysis [48] and Koopman modes [23,40]), the empirical eigenfunctions are orthogonal ($\mathbf{R}$ is self-adjoint), permitting expansion of (nominally) arbitrary fields onto the latter eigensystem. In addition, nonlinear stability assumes explicitly that the most energetic POD modes and instability modes are the same at least near the beginning of a supercritical Hopf bifurcation [32,33].

### 2.3. Dynamic Mode Decomposition

Dynamic Mode Decomposition (DMD) is a class of technique that has recently been introduced [40,45] for nonlinear systems analysis and reduction, which describe fluid flow structures based on Koopman modes [23,30,31]. DMD is an algorithm that approximates Koopman modes and eigenvalues. The algorithm is a variant of the standard Arnoldi algorithm that employs a linear operator defined for any nonlinear dynamical system that describes linear or nonlinear flow coherent structures. In addition, when DMD is applied to the linearized Navier–Stokes equations, Koopman modes reduce to linear global modes [12] and when DMD is applied to time-periodic flows, Koopman modes reduce to Fourier modes [40,5].

The algorithm presented by Schmid [45] will be used in what follows and is briefly described here. Given a data set of $(N+1)$ snapshots resolved in time, two different snapshots matrix can be constructed: $V_1^N$ (from the first to the $N$th snapshot) and $V_2^{N+1}$ (from the second to the $(N+1)$th snapshot). Assuming a linear mapping $A$ constant over the snapshot sequence that connects the flow field $u_i$ with the subsequent flow field $u_{i+1}$ ($u_{i+1} = Au_i$), it will be able to formulate the sequence of flow field as a Krylov sequence [52]

$$V_1^N = \{\mathbf{v}_1, A\mathbf{v}_1, A^2\mathbf{v}_1, \ldots, A^{N-1}\mathbf{v}_1\} \tag{9}$$

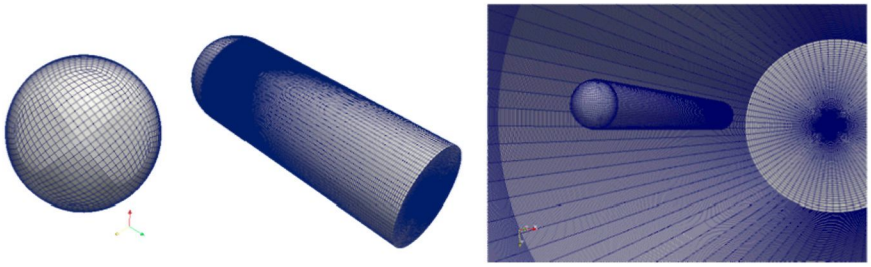

**Fig. 2.** Mesh M2 containing ~2 800 000 tetrahedral cells.

For a long data snapshots sequence, any further snapshots sequence can be expressed by linear combination of the previous ones:

$$V_2^{N+1} = AV_1^N = V_1^N S + re_{N-1}^T \tag{10}$$

where $S$ is a companion matrix, $r$ is the residual and $e_{N-1}$ the $(N-1)$th unit vector. The dynamic of the system is contained in matrix $A$, or its corresponding approximation matrix $S$. Matrix $S$ is determined by minimizing the residual $r$. Thus, an eigenvalue problem of matrix $S$ is solved ($S\mu = \lambda\mu$). DMD modes are then determined by the projection of the snapshots matrix $V_1^N$ over the eigenvectors $\mu$ of the companion matrix $S$.

This algorithm is not optimal to find eigenvalues and eigenvectors that describe the dynamics of the system, since it can be sensitive to noise [9] and even though the algorithm is analytically correct, it may be ill-conditioned in practice [45,5]. However it is a reasonably inexpensive method that has been proved to be effective in approximating linear eigenvalue problems [45], discrete Fourier transforms [5] and in capturing instability modes on nonlinear systems [1].

## 3. Direct Numerical Simulations

Three-dimensional Direct Numerical Simulations (DNS) have been performed to study the flow around a hemisphere-cylinder of aspect ratio $L/D = 8$ (where $L$ is the length of the body without including the radius of the nose and $D$ is the diameter of the body) at $AoA = 20^\circ$ and $Re = 1000$, the latter is defined as:

$$Re = \frac{U_\infty D}{\nu} \tag{11}$$

The numerical code used both for the DNS and to generate the base flow for the present analysis was OpenFOAM, an open source Computational Fluid Dynamics software (http://www.openfoam.com). High quality flow stability results over axisymmetric bodies have been obtained recently using this code by Bohorquez et al. [4,3] and Sanmiguel-Rojas et al. [43,42].

The employed OpenFOAM module discretizes the incompressible Navier–Stokes equations using a finite volume method. The spatial and temporal discretizations were performed using a central differencing scheme (for the convective and diffusive term) and a Crank–Nicholson scheme respectively, with second order of accuracy in both cases.

The computational domain was a coaxial cylindrical surface of diameter $20D$ and $50D$ long. This length was shown to be sufficient to accurately capture the physics of the problem in the case of $AoA = 0^\circ$ (Sanmiguel-Rojas et al. [43], Bohorquez et al. [4]) and was first also used in the present analysis. The mesh employed was composed of a regular tetrahedral grid with ~2.8 million cells. No-slip boundary conditions are employed on the body surface and free stream boundary conditions on the far-field. Fig. 2 shows the mesh and the computational domain.

Grid independence analysis was performed using a method introduced by Roache [37]. This method introduces $n$th-order methods to generalize Richardson extrapolation. Thus, an estimation of the grid independent solution is introduced by the grid convergence index, defined as

**Table 1**
Grid convergence study on the DNS.

| Mesh | Number of cells | $Cd$ | $GCI$ |
|---|---|---|---|
| M1 | 1 358 400 | 0.4269 | – |
| M2 | 2 833 120 | 0.4157 | 3.00 |
| M3 | 4 112 320 | 0.4135 | 0.59 |

$$GCI_{j+1,j}(\%) = 3\left|\frac{f_j - f_{j+1}}{f_j(l^n - 1)}\right| \cdot 100 \tag{12}$$

where $f_j$ is any field value discretized on the fine mesh (e.g. streamwise velocity $U_z$ in mesh M3), $f_{j+1}$ is the same field value discretized on the coarse mesh (e.g. streamwise velocity $U_z$ in mesh M2), $n$ is the order of the method and $l$ is the size refinement ratio in a coordinate direction from the fine to coarse grid (e.g. $N_{z,M3}/N_{z,M2}$, where $N_{z,M2}$ is the number of nodes in $z$ direction of mesh M2 and $N_{z,M3}$ in M3). The convergence ratio $R = (f_{j+1} - f_j)/(f_{j+2} - f_{j+1})$ must be in the interval $0 < R < 1$ in order to ensure monotonic convergence. More details about this method can be found in the literature [42,11]. The results of the grid convergence study are presented in Table 1. Three different grids have been employed: a small grid M1 with $\sim 1.4 \times 10^6$ cells, a medium grid M2 with $\sim 2.8 \times 10^6$ cells and a big grid M3 with $\sim 4.1 \times 10^6$ cells. The ratio between the fine and the coarse grid on the radial direction was the same, $l = 2^{1/1.7}$. The convergence ratio was $R = 0.19$ and the order of the method $n = 4.01$. $GCI$ values for the bigger grid and medium grid are small enough to prove that both meshes are close to the grid independence solution (the relative error is <3%), therefore, in order to reduce computational resources, the medium mesh has been selected to perform the numerical simulations.

## 4. Model description and experimental facility

The same flow conditions of the DNS have been reproduced on an experimental facility. Time-resolved Particle Image Velocimetry (PIV) experiments were carried out in the water tunnel of the Laboratory for Turbulence Research in Aerospace and Combustion (LTRAC) at Monash University [26]. The plane of measurements was the symmetry plane, parallel to the incoming flow, the Reynolds number 1000, the angle of attack 20° and the model aspect ratio $L/D = 8$.

The LTRAC water tunnel test section is 500 mm × 500 mm in cross-section and 5 m in length. The measurements were carried out downstream the LTRAC water tunnel, away from the contraction area in order to achieve optimum water quality. The free stream turbulent intensity is less than 1%.

To perform PIV, a Quantronix laser was employed, having up to 60 mJ per pulse. In order to guarantee that the studied phenomenon was highly resolved in time, flow frequency has to be more than twice Nyquist frequency, thus the laser frequency was

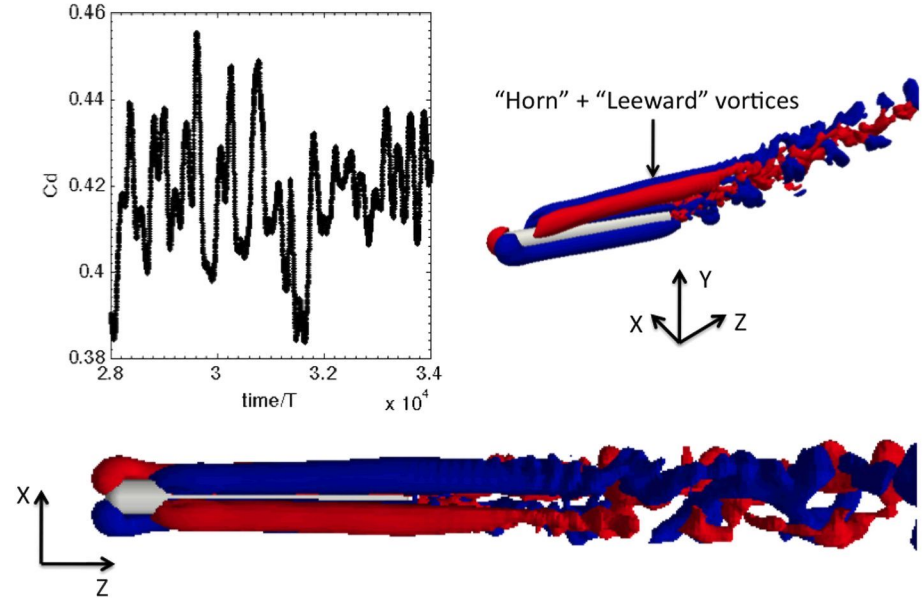


**Fig. 3.** Evolution of drag coefficient in time and iso-surface of instantaneous spanwise velocity ($U_x$) of DNS, time $t$ (s) non-dimensionalized with period $T = 0.0002$ s. Iso-surface values $U_x = \pm 0.08$, red and blue colors represent positive and negative values respectively. (For interpretation of the references to color in this figure legend, the reader is referred to the web version of this article.)

set to 250 Hz. Laser thickness was regulated with optical lenses that are set up to diverge and trim the laser sheet and it was 2 mm. The tunnel was seeded with 11 microns Potter's glass sphere with a density of 1.01 kg/m$^3$. Finally the camera employed was a PCO.Dimax camera equipped with 100 mm Zeiss Macro Lens. Magnification factor was 0.045 mm/pixel and the field of view of the experiment was 90 mm × 90 mm.

## 5. Results

Three-dimensional DNS and PIV experimental measurements have been combined around a hemisphere-cylinder at $Re = 1000$, $AoA = 20^\circ$ and $L/D = 8$. At these conditions flow is unsteady and three-dimensional massively separated, resulting in rather complex configurations. Fig. 3 presents evolution in time of drag coefficient and iso-surface of instantaneous spanwise velocity ($U_x$) obtained from the numerical simulations. The two pairs of antisymmetric vortices (horn and leeward vortices) emerging from the body upper surface predicted in the literature [20] are detected. At this flow condition these vortices are unsteady. In addition, the multiple peaks in the drag curve time-signal show that this unsteadiness is a consequence of a mixture of multiple frequencies.

Experiments were carried out on the symmetry plane on an area close to the nose of the body. It has been identified, the points in the plane in which the velocity fluctuations perpendicular to the body surface were zero. Power Spectral Density (PSD) analysis has been performed at these points, which represent the shear layer that is surrounding flow separation region. Fig. 4 (bottom) presents streamwise mean velocity flow and the stream lines on this plane. The square blue dots are the points on the shear layer, where the frequency analysis has been carried out. Fig. 4 (top left) presents the frequencies associated with the shear layer. The Strouhal number has been defined as $St = f \cdot \sin(AoA) \cdot D/U$, where $f$ is the frequency in Hz, $D$ is the diameter of the body, $D = 0.025$ m, and $U$ is the far-field streamwise flow velocity $U = 0.04$ m/s. Three (non-dimensional) frequencies are detected in this case $St \simeq 0.02$, $St \simeq 0.13$ and $St \simeq 0.24$. The (near-) exponential growth curves of these frequencies in the shear layer along the streamwise direction are represented in Fig. 4 (top right) [47]. An additional frequency is analyzed, $St \simeq 0.06$, since this frequency has been detected in some points of the shear layer. PSD amplification $a$ is non-dimensionalized with the amplification value $a_0$ obtained in the first spatial point $z_0$ for each case. On the other hand, the spatial component is non-dimensionalized with the initial and final points positions $z_0$ and $z_L$ respectively. The slopes of the exponential growth rate curves are very similar in all cases presented in Fig. 4 (top right). However the higher slope has been associated with the curve representing the frequency $St \simeq 0.13$. Therefore, this frequency is considered as the dominant frequency in the separation area, obtained from the experimental results. The same frequency has been detected by several authors in the literature in their studies of flow around a hemisphere-cylinder at different Reynolds numbers, zero and non-zero angles of attack [4], flow around bluff bodies [51] and flow around NACA profiles with angle of attack [39,38]. In all cases, this frequency has been associated with the von Karman vortex shedding. The frequencies $St \simeq 0.06$ and $St \simeq 0.24$ are considered as sub-harmonics and harmonics of the dominant frequency $St \simeq 0.13$.

### 5.1. Proper Orthogonal Decomposition

POD analysis has been performed on the DNS data. In order to focus attention on the separation region, the computational domain has been reduced to perform this analysis. The volume downstream the model has been removed and only a quarter of the total volume that surrounds the body was kept. This volume was selected in the region where separation and vortices are present. Results obtained on mesh M2 where restricted to mesh M1 in order to reduce computational costs. Barkley et al. [2] showed that the influence on the domain size over the eigenvalues computations was only through the base flow. Thus the dynamics and frequencies of a system can be accurately captured in smaller meshes using the base flow computed on larger meshes. The number of snapshots for this analysis was 300 and the separation in time between each snapshot $\Delta t = 0.005$ s.

Fig. 5 (top left) presents the kinetic energy (in %) associated with the 10 most relevant POD modes. Almost 50% of kinetic energy that is describing the total dynamic process is associated with each of the 2 most relevant POD modes, while a negligible small percentage of energy is distributed over all of the remaining POD

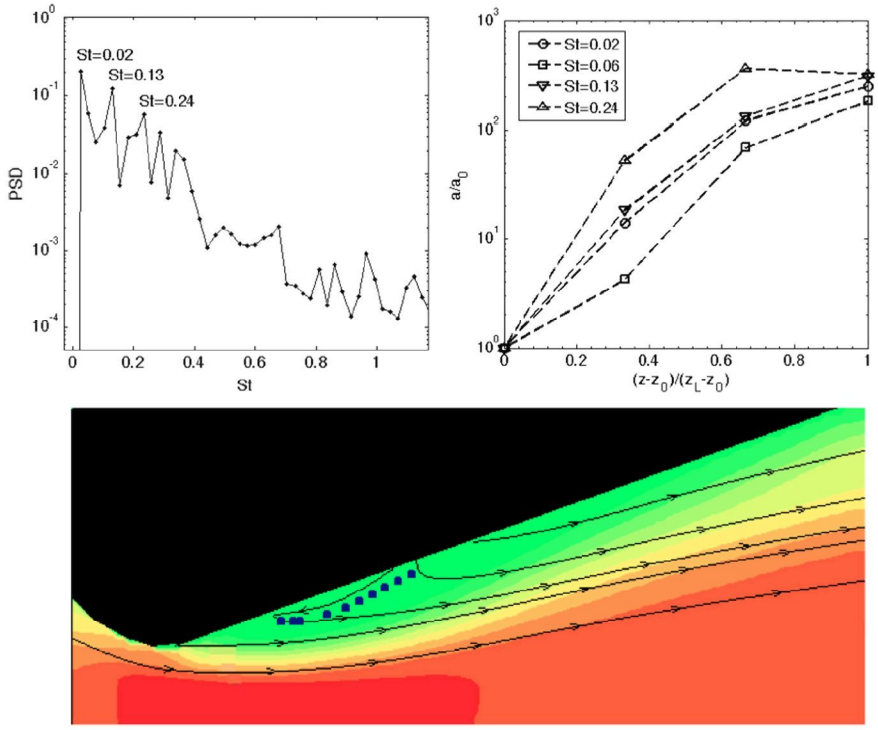


**Fig. 4.** PIV experimental results on symmetry plane. Top left: PSD frequency on shear layer, $St = f \cdot \sin(\alpha) \cdot D/U$. Top right: Exponential growth rate curves of different frequencies on shear layer points, $a/a_0$ is amplification and $(z - z_0)/(z_L - z_0)$ represents evolution in space along the streamwise direction. Bottom: Streamwise mean velocity flow and streamlines. Velocity is normalized with maximum velocity and 21 equidistant isolines are represented from $-1$ to 1. Blue, green and red colors are associated to $-1$, 0 and 1 velocity values respectively. Square blue dots represent shear layer points where frequencies have been calculated. (For interpretation of the references to color in this figure legend, the reader is referred to the web version of this article.)

modes. Energy is found to be distributed in pairs of modes with similar eigenvalues. Thus POD modes are traveling in pairs and the $n$th pair corresponds with the $n$th harmonic of the fundamental frequency [32]. When the flow is dominated by periodic vortex shedding, each pair of modes might correspond to flow oscillating structures. Fig. 5 (top right) presents the spanwise velocity component $U_x$ of the first and second POD modes. As it can be seen, they are the same mode phase-shifted by $\pi/2$. Fig. 5 (bottom) represents the PSD spectrum of the four most energetic POD time coefficients. In the four spectrums the same mixture of frequencies composes each POD mode. However, it is seen that the frequency $St \simeq 0.12$ is dominant in POD modes 1 and 2 and that the frequency $St \simeq 0.24$ is dominant in POD modes 3 and 4. These frequencies correspond with the dominant frequency and its first harmonic, respectively. The influence of the harmonics over the spatial structure of the POD eigenmode is not relevant. The dominant frequency $St \simeq 0.12$ was also detected on the experimental results of Fig. 4 and was associated with the oscillations in the separation bubble.

### 5.2. Dynamic Mode Decomposition

DMD analysis has been performed on the DNS data. As it was done for the POD analysis, in order to focus attention on the separation area, the computational domain has been reduced and the results from mesh M2 were restricted to mesh M1. The control volume on which the analysis has been performed, is the same as for POD analysis. The number of snapshots used for this analysis was ~600, approximately twice the number of snapshots used for the POD analysis. However, in this case, the separation in time between each snapshot was chosen to be the same than the snapshots separation for POD, $\Delta t = 0.005$ s.

Fig. 6 (left) shows the eigenvalues associated with the dominant DMD modes (and its *c.c.*). They are the higher exponential growth

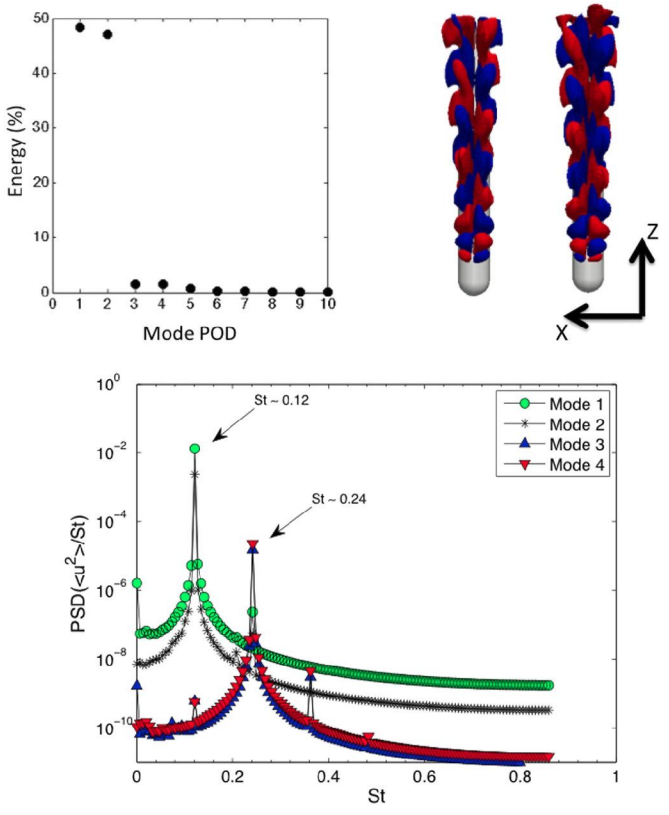


**Fig. 5.** POD performed to the DNS. Top left: Energy associated with the 10 most dominant POD modes. Top right: (from left to right) First and second POD modes in spanwise velocity $U_x$. Iso-surface values $U_x = \pm 0.03$, red and blue colors represent positive and negative values respectively. Bottom: POD performed to the DNS. PSD of the 4 most dominant POD modes, $St = f \cdot \sin(\alpha) \cdot D/U$. (For interpretation of the colors in this figure, the reader is referred to the web version of this article.)

rate modes [41,40]. These modes correspond with the three leading transient Koopman modes detected by Bagheri [1] when he studied the flow around a cylinder on the limit cycle period of oscillations at critical Reynolds number. Bagheri [1] associated the two oscillatory modes with the von Karman vortex shedding. Fig. 6 (right) presents iso-surface of spanwise velocity $U_x$ of the three modes detected. The first mode is associated with the eigenvalue $\lambda = 0$ ($St = 0$) and represents the time-averaged mean flow. This mode is associated with the couples of horn and leeward vortices already described in Fig. 3. The second mode $\lambda = i\omega$ ($St \simeq 0.12$) is associated with the fundamental frequency $\omega$. Finally, the third mode $\lambda = i2\omega$ ($St \simeq 0.24$) corresponds to the first harmonic of the fundamental frequency. The wave length of this mode is half of the wave length of the dominant mode $St \simeq 0.12$. This mode appears as consequence of the interaction of the nonlinear terms with themselves [1].

Fig. 7 (up left) presents the DMD steady mode in detail. Iso-surface of spanwise velocity $U_x$ shows the two antisymmetric rotating vortices horn and leeward vortices. Fig. 7 (up right) presents the DMD mode associated with the fundamental frequency $St \simeq 0.12$ in detail. Iso-surfaces of velocity $U_x$, $U_y$ and $U_z$ (from left to right) show that this mode is associated with flow separation. In addition, the structure of the leeward vortices is visible on the three velocity components. Streamwise velocity $U_z$ shows a different character of POD mode in the area very close to the nose of the body, related with the separation bubble. As the POD mode evolves farther from the bubble, the structures associated with the oscillation of the vortices and the wake, become apparent.

To complete the analysis DMD has been performed on the experimental data at the symmetry plane of the body. The number of snapshots used for this analysis was ~2000 and the value of the time interval between each snapshot was $\Delta T = 1/250 = 0.004$ s (250 Hz being the laser frequency of the PIV system). Fig. 7 shows the streamwise velocity and the subsequent perpendicular velocity component of the DMD mode associated with the dominant frequencies $St \simeq 0.12$. Once more it is evident that this mode corresponds to a shear layer instability. In addition, the good qualitative agreement between experimental and numerical results is further underlined.

Finally, DMD and POD modes obtained from the DNS are compared. Fig. 8 (left) shows the iso-surfaces of the three velocity components (from left to right) $U_x$, $U_y$ and $U_z$ of the DMD mode associated with the dominant frequency $St \simeq 0.12$, while Fig. 8

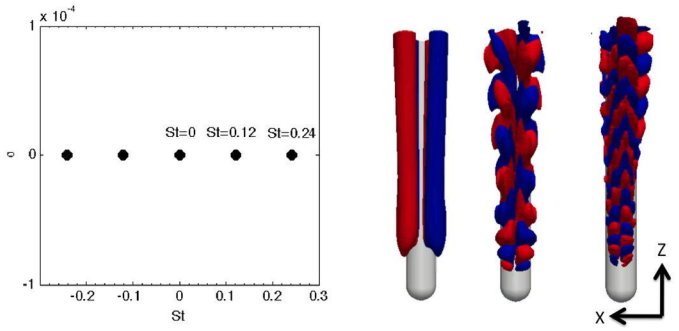


**Fig. 6.** DMD performed to the DNS. Left: DMD dominant modes eigenvalues. Right: DMD dominant modes eigenfunctions in spanwise velocity $U_x$. Iso-surface values (from left to right) $U_x = \pm 2.5$ for the steady mode $St = 0$ and $U_x = \pm 0.03$ for modes $St \simeq 0.12$ and $St \simeq 0.24$, $St = f \cdot \sin(\alpha) \cdot D/U$. Red and blue colors represent positive and negative values respectively. (For interpretation of the colors in this figure, the reader is referred to the web version of this article.)

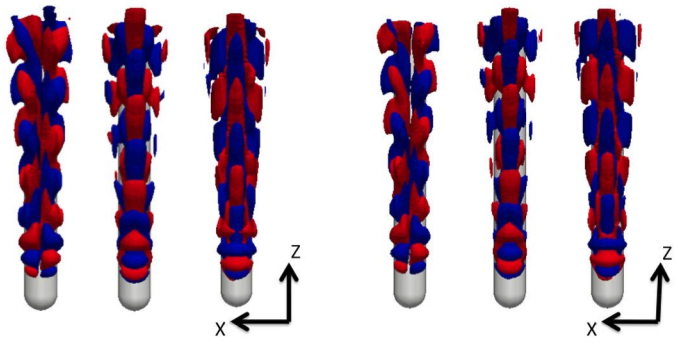


**Fig. 8.** Left: DMD mode $St \simeq 0.12$, from left to right iso-surface $\pm 0.03$ of $U_x$, $U_y$, $U_z$. Right: POD first mode, from left to right iso-surface $\pm 0.03$ of $U_x$, $U_y$, $U_z$. Red and blue colors represent positive and negative values respectively. (For interpretation of the colors in this figure, the reader is referred to the web version of this article.)

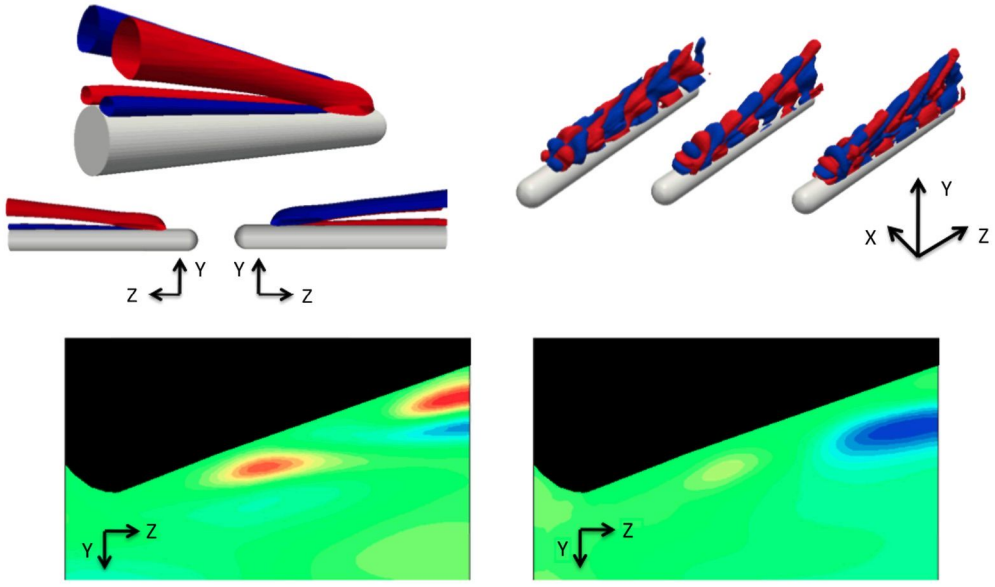


**Fig. 7.** DMD performed on DNS (top) and PIV (bottom) results. Top left: DMD steady mode, iso-surface $U_x = \pm 2.5$. Top right: DMD mode $St \simeq 0.12$, from left to right iso-surface $\pm 0.03$ of $U_x$, $U_y$, $U_z$. Red and blue colors represent positive and negative values respectively. Bottom: DMD mode on symmetry plane of PIV results. $U_z$ and $U_y$ velocity fields are normalized with maximum values of $U_z$ and $U_y$ respectively. 21 equidistant isolines from $-1$ to 1. Blue, green and red colors are associated to $-1$, 0 and 1 velocity values respectively. (For interpretation of the colors in this figure, the reader is referred to the web version of this article.)

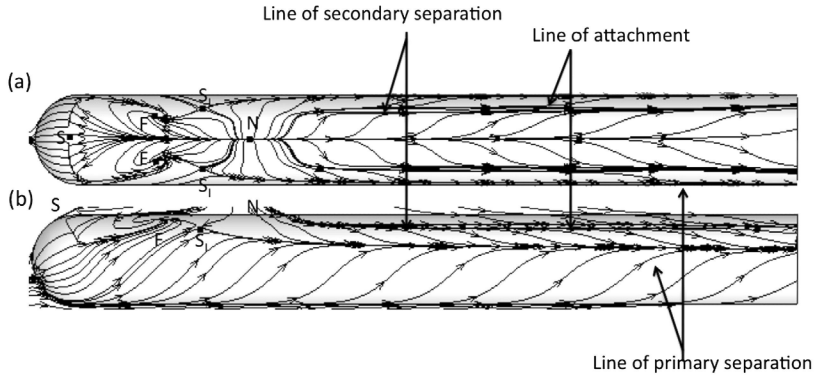


**Fig. 9.** Top: Surface streamlines and critical points on the hemisphere cylinder on the plane $X-Z$ (parallel to separation bubble). Bottom: Surface streamlines and critical points on the hemisphere-cylinder on the plane $Y-Z$ (parallel to symmetry plane).

(right) shows the same velocity components of the first POD mode. The coincidence of the frequencies of the DMD and POD modes shown in Fig. 5, $St \simeq 0.12$, together with the spatial analogies of the amplitude functions of all components of velocity of the DMD and POD modes, suggest that the two techniques reveal the same. There is a clear relationship between the oscillations present in the separation bubble and in the system of horn and leeward vortices. Recalling that nonlinear stability assumes explicitly that at least near the beginning of a supercritical Hopf bifurcation, the most energetic POD modes and instability modes are the same [32,33], this result suggests that the structure of the leading flow eigenmode is expected to be very similar to that revealed herein by the DMD and POD analysis. The finding of the dominant frequency $St \simeq 0.12$ is in good agreement with the literature [51,44,39,38,42], in which a von Karman instability is associated with such frequency. As a consequence, these results suggest that the dominant mechanism associated with flow separation may be associated with an instability within the leeward vortices.

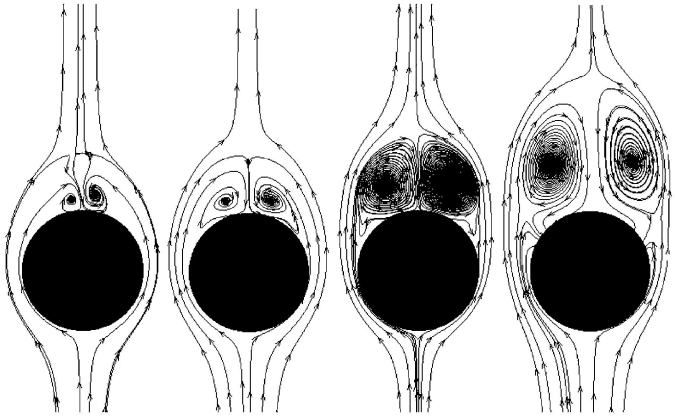

**Fig. 10.** Streamlines on a set of $XY$ planes along $Z$ axis (streamwise direction) in $Z/L = 0.15, 0.25, 0.5, 1$, considering $Z = 0$ the junction point between the semisphere and the cylinder.

### 5.3. Flow topology

In order to completely characterize the complex flow pattern caused by three-dimensional separation, critical point theory has been applied to the hemisphere cylinder body surface DNS data. Topological patterns found by Tobak and Peake [50], who studied the flow around the same geometry at angle of attack 10° and Reynolds number $10^6$, have been reproduced by the present DNS results. Fig. 9 (upper) shows the surface stream lines and critical points on the hemisphere cylinder on the plane $X-Z$ (parallel to separation bubble), while Fig. 9 (lower) shows the surface stream lines and critical points on the plane $Y-Z$ (parallel to symmetry plane). The critical points and the surface streamlines identify three different topology patterns: the separation bubble, the horn vortices and the leeward vortices (primary and secondary). The separation bubble is defined by the following critical points: the saddle of separation ($S$), the node of re-attachment ($N$), and two foci ($F$) and two saddles $S_{II}$ symmetrically positioned respect to the symmetry plane. Reversed flow within the separation bubble is marked out by the saddle ($S$) and the node ($N$), located in the symmetry plane. The three-dimensional separation bubble extends over the nose surface of the body and is limited by two unstable foci points ($F_I$). The two horn vortices detected in Fig. 3 are emerging perpendicularly from these two focal points. A line of separation is originated downstream the node $N$, while the saddle point $S_{II}$ is the origin of the line of re-attachment. These two lines evidence the presence of the coupled system of the horn and leeward vortices downstream the separation bubble. These vortices were predicted in Fig. 3 and in the DMD analysis of Fig. 6 (top left). Leeward vortices appear as a result of cross-flow, that causes boundary layer to separate and roll up. Additionally, it is possible to evidence the lines of secondary separation, associated with a new pair of vortices, the secondary leeward vortices.

Finally, the spatial evolution of the horn and leeward vortices has been studied in four transversal planes along the body surface. The location of the planes along $Z$ axis (streamwise direction) are $Z/L = 0.15$, 0.25, 0.5, 1, considering $Z = 0$ the junction point between the hemisphere and the cylinder. Fig. 10 presents streamlines on the different planes mentioned before. The coupled pattern of horn and leeward vortices is present in all cases. The vortices size increases with the distance from the nose of the body. These vortices are unsteady. In planes $Z/L = 0.25$, 0.5, 1 it is evidenced the presence of the secondary leeward vortices, associated with the surface streamlines of secondary separation. These vortices are continuously interacting with the coupled system of horn and leeward vortices. Finally, in plane $Z/L = 1$ a new pattern is present. Flow emerging from the lower part of the body surface is appearing and finally mixing up with the pairs of vortices mentioned before.

Power Spectral Density (PSD) analysis has been performed over the 4 transversal planes previously mentioned, in 5 different points. These points are shown in Fig. 11 (top left). As it is seen, they are located close to the body surface and in the area of the vortices system. The three velocity components present a saturated oscillatory movement in all cases. Fig. 11 (top right) shows an example of these oscillations. The frequencies detected in points Pt1 and Pt2 are equal. In these two points, two different dominant frequencies were detected in planes $Z/L = 0.15, 0.25, 0.5$: $St \simeq 0.01$ and $St = 0.07$. In plane $Z/L = 1$ both frequencies were found in Pt2, but only the higher frequency $St \simeq 0.07$ was detected in Pt1. In

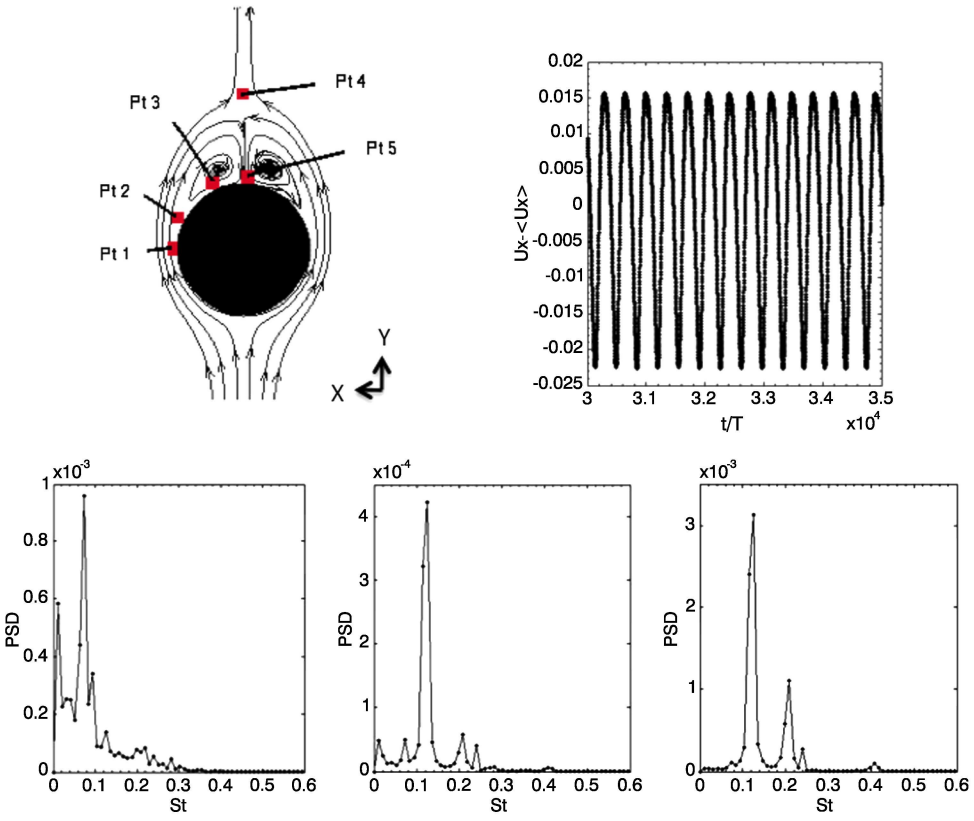


**Fig. 11.** PSD on $XY$ planes along $Z$ axis. Top left: Points of application of FFT, Pt1 = (0.0126, 0, $Z/L$), Pt2 = (0.0126, 0.006, $Z/L$), Pt3 = 0.006, 0.0126, $Z/L$, Pt4 = (0, 0.03, $Z/L$), Pt5 = (0, 0.0126, $Z/L$). Hemisphere-cylinder diameter $D \in [-0.0125, 0.0125]$. Top right: Spanwise velocity $U_x$ in Pt5, $Z/L = 0.25$. Mean spanwise velocity $\langle U_x \rangle$ and time $t$ non-dimensionalized with period $T = 0.0002$. Bottom (from left to right): PSD in Pt2, Pt3 and Pt5.

points Pt3, Pt4 and Pt5 a single dominant frequency $St \simeq 0.12$ was found in all planes. An example of these PSD diagrams is presented in Fig. 11 (bottom). From left to right it is shown PSD in points Pt2, Pt3 and Pt5 in plane $Z/L \simeq 0.25$. The frequency range captured in all cases is in good agreement with the values of the frequency spectrum shown on the experiments of Fig. 4. The oscillation of the coupled system of vortices (horn and leeward) is driven by the fundamental frequency $St \simeq 0.12$ and its sub-harmonic $St \simeq 0.06$.

Finally, in order to see the vortex movement in time, the time-evolution of streamlines in plane $Z/L = 1$ is presented in Fig. 12 within one oscillation period. The time reference is the frequency $St = 0.12$ and the evolution of streamlines is shown at time $t = T$, $t \simeq T/4$ and $T \simeq T$. The periodic character quantified above is visible in these images.

The finding in both, experimental and numerical results of a single dominant frequency leading the oscillations in the system of vortices at very low studied Reynolds number (1000), may suggest that the origin of the dominant mechanism of oscillation associated with flow separation could be a instability found in the horn and leeward vortices.

## 6. Conclusions

Three-dimensional numerical simulations and PIV experiments have been combined in order to study the three-dimensional separation effects that appear on a hemisphere-cylinder at Reynolds number $Re = 1000$, with aspect ratio $L/D = 8$ and angle of attack $AoA = 20°$. The flow was found to be nonlinear and unsteady. Unsteady separation at these flow conditions gives rise to a pair of asymmetric and unsteady vortices in the surroundings of the separation bubble.

As a first step of the analysis, Discrete Fourier Transform has been performed in order to compare experimental and numerical results, which were found to be in good agreement. A single dominant frequency was detected, $St \simeq 0.12$, and it was associated with the horn and leeward vortices system and with the oscillations within the separation area. The same frequency was found by other authors who studied the flow past axisymmetric bodies [4,51]. They associated that frequency with the von Karman vortex shedding. It suggests that the dominant mechanism of oscillation within the bubble may be driven by a vortices instability.

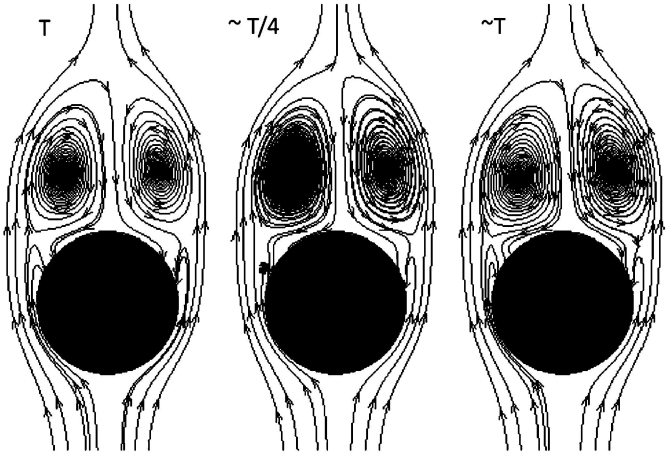


**Fig. 12.** Streamlines in plane $Z/L = 1$ at period $T$, $\simeq T/4$ and $\simeq T$.

Subsequently, POD and DMD techniques have been applied for the first time in tandem, in order to elucidate flow physics at these conditions. As it was expected, POD modes were found to travel in pairs. When the flow is dominated by periodic vortex shedding, each pair of modes might correspond to flow oscillating structures [32]. More than 90% of kinetic energy was concentrated on the

first pair of POD modes. These modes were oscillating with a frequency equal to the dominant frequency detected on experimental results, $St \simeq 0.12$. On the other hand, DMD analysis captured three leading transient Koopman modes: a steady and two oscillatory modes. The steady mode was representing a pair of unsteady vortices called horn and leeward vortices. The two oscillatory modes (and their *c.c.*) were oscillating with fundamental frequency and its corresponding first harmonic. They were compared with the von Karman vortex shedding modes obtained on a flow past a cylinder at critical Reynolds number on the limit cycle period of oscillations also delivering a fundamental frequency of the DMD mode of $St \simeq 0.12$ [1]. Both POD and DMD modes were equal and they were composing a single system of flow oscillations containing the separation bubble and the horn and leeward vortices.

Finally, different structural flow patterns caused by flow separation have been identified using critical-point analysis on the surface of the body: separation bubble and the pair of vortices system composed by the horn and the leeward vortices. Horn vortices emerge perpendicularly from two unstable foci points located on the surface, while separation bubble is marked out by a saddle and a node points that appear on the symmetry plane, on the body surface. On the other hand, separation and attachment lines evidence the presence of the horn and leeward vortices system downstream the separation bubble. Finally, analysis performed on a set of planes perpendicular to the inflow direction demonstrated that leeward vortices appear as a system that is continuously interacting with the horn vortices. PSD has been performed in different points close to the body surface and inside the vortex area in all these four planes. The dominant frequency $St \simeq 0.12$ was found in the symmetry plane and close to the vortex pattern further underlying the full characterization of the dominant flow feature at these conditions.

## Conflict of interest statement

None declared.

## Acknowledgements

Support of the Marie Curie Grant PIRSES-GA-2009-247651 *"FP7-PEOPLE-IRSES: ICOMASEF – Instability and Control of Massively Separated Flows"* is gratefully acknowledged. Support of the Spanish Ministry of Science and Innovation through Grant TRA2012-34148 *"Mejoras del Rendimiento aerodinámico de alas mediante control de mecanismos de inestabilidad global"* is gratefully acknowledged. Support of the Defense Science and Technology Organization of Australia is gratefully acknowledged. This work was supported by the Multi-modal Australian ScienceS Imaging and Visualisation Environment (MASSIVE) (www.massive.org.au).

## References

[1] S. Bagheri, Koopman-mode decomposition of the cylinder wake, J. Fluid Mech. 726 (2013) 596–623.
[2] D. Barkley, R.D. Henderson, Three-dimensional Floquet stability analysis of the wake of a circular cylinder, J. Fluid Mech. 322 (1996) 215–241.
[3] P. Bohorquez, L. Parras, Three-dimensional numerical simulation of the wake flow of an afterbody at subsonic speeds, Theor. Comput. Fluid Dyn. 27 (2012) 201–218.
[4] P. Bohorquez, E. Sanmiguel-Rojas, A. Sevilla, J. Jimenez-Gonzalez, C. Martinez-Bazan, Stability and dynamics of the laminar wake past a slender blunt-based axisymmetric body, J. Fluid Mech. 676 (2011) 110–144.
[5] K.K. Chen, J.H. Tu, C. Rowley, Variants of dynamic mode decomposition: boundary condition, Koopman, and Fourier analyses, J. Nonlinear Sci. 22 (6) (2012) 887–915.
[6] C.E. Costis, N.T. Hoang, D.P. Telionis, Laminar separating flow over a prolate spheroid, J. Aircr. 26 (1989) 810–816.
[7] C.E. Costis, D.P. Telionis, Unsteady vortical wakes over a prolate spheroid, AIAA J. 20 (1983) 1189–1193.
[8] U. Dallmann, Topological structures of three-dimensional flow separations, 1982, DFVLR-IB 221-82 A07.
[9] D. Duke, J. Soria, D. Honnery, An error analysis on the dynamic mode decomposition, Exp. Fluids 52 (2012) 529–542.
[10] B. Fairlie, Flow separation on bodies of revolution at incidence, in: 7th Australian Hydraulics and Fluid Mechanics Conference, Brisbane, 18–22 August 1980, pp. 18–22.
[11] J.H. Ferziger, M. Perić, Computational Methods for Fluid Dynamics, Springer-Verlag, Berlin, 2002.
[12] F. Gomez, S. Le Clainche, P. Paredes, M. Hermanns, V. Theofilis, Global linear instability at the dawn of its 4th decade: recent progress and remaining challenges, AIAA J. 50 (12) (2012) 2731.
[13] A. Gross, C. Jagadeesh, H. Fasel, Numerical investigation of three-dimensional separation on axisymmetric bodies at angle of attack, AIAA Paper 2012-0098, 2012.
[14] N. Hoang, O. Rediniotis, D. Telionis, Symmetric and asymmetric separation patterns over a hemisphere cylinder at low Reynolds number and high incidences, J. Fluids Struct. 11 (1997) 793–817.
[15] N. Hoang, O. Rediniotis, D. Telionis, Hemisphere cylinder at incidence at intermediate to high Reynolds numbers, AIAA J. 37 (1999) 1240–1250.
[16] P. Holmes, J. Lumley, G. Berkooz, Turbulence Coherent Structures, Dynamical Systems and Symmetry, Cambridge University Press, 1996.
[17] H. Hornung, A.E. Perry, Some aspects of three dimensional separation, part I: streamsurface bifurcations, Z. Flugwiss. Weltraumforsch. 8 (1984) 77–87.
[18] T. Hsieh, Hemisphere-cylinder in low supersonic flow, AIAA J. 13 (1975) 1551–1552.
[19] T. Hsieh, An investigation of separated flow about a hemisphere-cylinder at incidence in the Mach number range from 0.6 to 1.5, AIAA Paper 77-179, 1977.
[20] T. Hsieh, K. Wang, Three-dimensional separated flow structure over a hemisphere-cylinder, J. Fluid Mech. 324 (1996) 83–108.
[21] J.I. Jiménez-González, E. Sanmiguel-Rojas, A. Sevilla, C. Martínez-Bazán, Laminar flow past a spinning bullet-shaped body at moderate angular velocities, J. Fluids Struct. 43 (November 2013) 200–219, http://dx.doi.org/10.1016/jjfluidstructs201307001.
[22] I.T. Jolliffe, Principal Component Analysis, Springer, New York, NY, 1986.
[23] B.O. Koopman, Hamiltonian systems and transformations in Hilbert space, Proc. Natl. Acad. Sci. USA 17 (1931) 315–318.
[24] H. Kreplin, H. Vollmers, H. Meier, Measurements of the wall shear stress on an inclined prolate spheroid, Z. Flugwiss. Weltraumforsch. 6 (1982) 248–252.
[25] W. Krzanowski, Selection of variables to preserve multivariate structure, using principal components, Appl. Stat. 36 (1987) 22–33.
[26] S. Le Clainche, J. Li, V. Theofilis, J. Soria, Comparison of time-resolved particle image velocimetry and stability analysis on a hemisphere-cylinder, in: 42nd AIAA Fluid Dynamics Conference and Exhibit, New Orleans, USA, June 25–28, 2012.
[27] J. Lumley, The structure of inhomogeneous turbulent flows, in: A. Yaglom, V. Tatarski (Eds.), Atmospheric Turbulence and Radio Wave Propagation, 1967.
[28] A. Meade, L. Schiff, Experimental study of three-dimensional separated flow surrounding a hemisphere-cylinder at incidence, AIAA Paper 87-2492, 1987.
[29] H. Meier, H. Kreplin, Experimental investigations of boundary layer transition and separation on a body of revolution, Z. Flugwiss. Weltraumforsch. 4 (1980) 65–71.
[30] I. Mezic, Spectral properties of dynamical systems, model reduction and decompositions, Nonlinear Dyn. 41 (2013) 309–325.
[31] I. Mezic, Analysis of fluid flows via spectral properties of the Koopman operator, Annu. Rev. Fluid Mech. 45 (2013) 357–378.
[32] B. Noack, K. Afanasiev, M. Morzynski, G. Tadmor, F. Thiele, A hierarchy of low-dimensional models for the transient and post-transient cylinder wake, J. Fluid Mech. 497 (2003) 335–363.
[33] K. Oberleithner, M. Sieber, C.N. Nayer, C.O. Paschereit, C. Petz, H.C. Hege, B. Noack, I. Wygnansky, Three-dimensional coherent structures in a swirling jet undergoing vortex breakdown: stability analysis and empirical mode construction, J. Fluid Mech. 679 (2011) 383–414.
[34] D. Peake, M. Tobak, Three-dimensional flows about simply components at angle of attack, in: NASA Technical Memorandum, 1992, 84226.
[35] A. Perry, M. Chong, A description of eddying motions and flow patterns using critical-point concepts, Annu. Rev. Fluid Mech. 19 (1987) 125–155.
[36] A.E. Perry, H. Hornung, Some aspects of three dimensional separation, part II: vortex skeleton, Z. Flugwiss. Weltraumforsch. 8 (1984) 155–160.
[37] P.J. Roache, Perspective: a method for uniform reporting of grid refinement studies, J. Fluids Eng. 116 (1994) 405.
[38] D. Rodríguez, V. Theofilis, Structural changes of laminar separation bubbles induced by global linear instability, J. Fluid Mech. 655 (2010) 280–305.
[39] D. Rodríguez, V. Theofilis, On the birth of stall cells on airfoils, Theor. Comput. Fluid Dyn. 25 (1–4) (2011) 105–118.
[40] C.W. Rowley, I. Mezic, S. Bagheri, P. Schlatter, D. Henningson, Spectral analysis of nonlinear flows, J. Fluid Mech. 641 (2009) 115–127.
[41] C.W. Rowley, I. Mezic, S. Bagheri, P. Schlatter, D. Henningson, Reduced-order models for flow control: balanced models and Koopman modes, in: Seventh IUTAM Symposium on Laminar–Turbulent Transition, Stockholm, Sweden, 23–29 June 2009.

[42] E. Sanmiguel-Rojas, J.I. Jiménez-González, P. Bohorquez, G. Pawlak, C. Martínez-Bazán, Effect of base cavities on the stability of the wake behind slender blunt-based axisymmetric bodies, Phys. Fluids 23 (2011) 114103.
[43] E. Sanmiguel-Rojas, C. Martínez-Bazán, J.M. Chomaz, Global mode analysis of axisymmetric bluff-body wakes: stabilization by base bleed, Phys. Fluids 21 (2009) 114102.
[44] G. Schewe, Reynolds-number effects in flow around more-or-less bluff bodies, J. Wind Eng. Ind. Aerodyn. 89 (2001) 1267–1289.
[45] P.J. Schmid, Dynamic mode decomposition of numerical and experimental data, J. Fluid Mech. 656 (2010) 5–28.
[46] L. Sirovich, Turbulence and the dynamics of coherent structures, parts I–III, Q. Appl. Math. 45 (1987) 561.
[47] J. Soria, J. Wu, The character of the instability of the separated shear layer from a square leading edge flat plate, in: 11th Australian Fluid Mechanics Conference, University of Tasmania, Hobart, Australia, 14–18 December 2002.
[48] V. Theofilis, Global linear instability, Annu. Rev. Fluid Mech. 43 (2011) 319–352.
[49] M. Tobak, D. Peake, Topology of two-dimensional separated flows, Annu. Rev. Fluid Mech. 14 (1992) 61–85.
[50] M. Tobak, D. Peake, Topology of two-dimensional and three-dimensional separated flows, AIAA Paper 79-1480, 1979.
[51] A.G. Tomboulides, S.A. Orszag, Numerical investigation of transitional and weak turbulent flow past a sphere, J. Fluid Mech. 416 (2000) 45–73.
[52] L.N. Trefethen, D. Bau, Numerical Linear Algebra, SIAM, 1997.
[53] X. Tricoche, Vector and tensor field topology simplification, tracking and visualization, PhD thesis, Universität Kaiserslautern, 2002.
[54] K. Wang, T. Hsieh, Separation patterns and flow structures about a hemisphere-cylinder at high incidence, AIAA Paper 92-2712, 1992.
[55] S.X. Ying, L.B. Schiff, J.L. Steger, A numerical study of three-dimensional separated flow past a hemisphere cylinder, AIAA Paper 87-1207, 1987.
[56] S.X. Ying, J.L. Steger, L.B. Schiff, D. Baganoff, Numerical simulation of unsteady viscous, high-angle-of-attack flows using a partially flux-split algorithm, AIAA Paper 86-2179, 1986.